Materials Research Proceedings 41 (2024) 2355-2363 https://doi.org/10.21741/9781644903131-259

Eigenstrain method in simulations of laser peen forming of curved surfaces

POLTL Dominik[1,a,*], TEJA SALA Siva[2,b], KASHAEV Nikolai[2,c] and KLUSEMANN Benjamin[1,2,d]

[1] Institute of Production Technology and Systems, Leuphana University Lüneburg, Germany

[2] Institute of Materials Mechanics, Helmholtz-Zentrum Hereon, Geesthacht, Germany

[a] dominik.poeltl@leuphana.de, [b] siva.sala@hereon.de, [c] nikolai.kashaev@hereon.de, [d] benjamin.klusemann@leuphana.de

Keywords: Finite Element Analysis, Laser Peen Forming, Eigenstrain, Bending, Curvature

Abstract. The eigenstrain ansatz allows for the efficient simulation of large-scale applications of Laser Peen Forming (LPF) while being subject to geometric constraints. A setup to investigate the viability of the method for non-uniform curvature is proposed. A small-scale laser processing is simulated on cylinder shells of given curvature. Eigenstrains are determined in representative cells and mapped onto a second cylinder shell with different curvature to simulate a large-scale processing operation. The eigenstrains result in changes in local curvature. This is repeated for four curvatures. The resulting data is used to investigate the dependence of the induced curvature change on the origin geometry of the eigenstrains. A determined regression relation provides insight into the feasibility of the eigenstrain ansatz beyond its constrains.

Introduction

The titanium alloy Ti-6Al-4V offers the aerospace industry a material with a high strength to weight ratio and excellent high temperature stability. This makes it the most used titanium alloy, but poses some challenges due to its difficult formability [1]. Laser Shock Peening (LSP) and its adaption for small forming operations, Laser Peen Forming (LPF) offers a highly controllable processing method: A pulsed high-energy laser hits a specimen perpendicular to its surface in a repeated, structured manner, thus creating a peening pattern that consists of a high number of individual shots based on parameters such as the shot diameter, the overlap of consecutive shots as well as the dimensions of the peened region. Each individual laser pulse, with an energy density in the order of magnitude GW/cm² and a duration in the ns scale, generates a rapidly expanding plasma on specimen's surface. This plasma in a water confined regime induces mechanical shock waves that propagate through the specimen, causing dynamic yielding and resulting in a plastic strain field [2], [3]. The induced local deformation leads to difference between initial and post-processing curvature.

For modelling of LPF, the direct simulation of a large number of peening shots is computationally very costly. An efficient shortcut for simulation of LPF is the use of the eigenstrain method, as presented by Hu and Grandhi [4]. Investigating laser peening of planar samples, Hu and Grandhi [4] used the periodicity of the in-plane plastic strain field to determine eigenstrains ε_p in representative volumes. Eigenstrains are strains that persist in a specimen without external loading, e.g. thermal strains. The eigenstrains are associated with representative positions in a peening patch. Once determined in a small-scale simulation, the eigenstrains can be mapped onto a large-scale geometry whose peening pattern can be much bigger than on the small-scale geometry. On this larger pattern, the eigenstrains ε_{ij} are introduced as anisotropic thermal expansion coefficients α_{ij} via

$$\begin{bmatrix} \varepsilon_{rr} & \varepsilon_{rt} & \varepsilon_{ra} \\ \square & \varepsilon_{tt} & \varepsilon_{ta} \\ \square & \square & \varepsilon_{aa} \end{bmatrix} = \Delta T \begin{bmatrix} \alpha_{rr} & \alpha_{rt} & \alpha_{ra} \\ \square & \alpha_{tt} & \alpha_{ta} \\ \square & \square & \alpha_{aa} \end{bmatrix} \quad (1)$$

in a notation for cylindrical coordinates and $\Delta T = 1K$. The use of the ansatz is not exclusive to LPF, as Faucheux et al. [5] demonstrated it for shot peening. Keller et al. [6] used the eigenstrain ansatz to investigate the influence of LSP on fatigue crack propagation rate. Sala et al. [7] used the method to build a database of arbitrary peening patterns to train a neural network on the prediction of the pattern based on the deformation. However, on the use of eigenstrains on curved geometries, only few studies exist. For instance, Cai and Zhang [8] transformed the determined eigenstrains with respect to the normal to an arbitrarily curved surface.

In this work, the term *source* is coined for the small-scale geometry that is the origin of the eigenstrains while the term *target* is coined for the large-scale geometry that is the destination of the eigenstrains. The main focus of this work will be the investigation of the influence of the difference of local curvature between the source and the target geometry. Other than a plane sheet, which trivially has the uniform curvature $\kappa_{planar} = 0\ \mathrm{mm}^{-1}$, only the cylinder shell features a uniform curvature: For a cylinder shell of outer radius r, the curvature is

$$\kappa(r) = r^{-1}. \quad (2)$$

Simulation setup

Specimen geometry. In this work, five discrete values of initial curvature are investigated, namely $\kappa \in \{10, 12, 14, 16, 20\} \cdot 10^{-3}\mathrm{mm}^{-1}$. This corresponds to five discrete radii of cylinder shell cuts. For each curvature, the source geometry is a 50 mm × 50 mm × 1 mm sheet bent to the corresponding outer radius. The target geometry is a 80 mm × 20 mm × 1 mm sheet that features the same radius. In order to describe the resulting strain fields via a common cylindrical coordinate system, all geometries are centered around the same origin and oriented along the same axis. As boundary conditions, the source geometry features one slim face with dimensions 50 mm× 1 mm with a prescribed encastre, as shown in Fig. 1. In contrast, the target geometry is fixed in the initial length of 10 mm. Figure 1 shows source and target geometries for two exemplary curvatures, including the corresponding boundary conditions. Using the commercial software package for Finite Element Method (FEM) simulations ABAQUS, continuous 8-node 3D elements with reduced integration and hourglass control (C3D8R) are used to mesh all geometries. For the source geometry, the peened region is meshed with and in-plane average element edge length of 0.1 mm. The target geometry features an in plane average element edge length of 0.2 mm. For both geometries, the thickness is discretized with 20 layers of elements, guaranteeing a fine enough discretization of the in-depth stress and strain fields.

Peening pattern. In the center of each source geometry, a peening pattern consisting of 4×4 laser shots is modelled. Each shot has a diameter of 3 mm. In order to model the angle of attack in industrial LSP systems, each circular spot is distorted to an ellipsis. The pattern exhibits an alternating row offset. Due to its structured generation, the pattern exhibits periodicity. This allows for the identification of representative cells. In this work, nine patches, namely one center patch (*C*) and eight wind rose patches (*N, NE, E* and so on), make up the set of the representative cells. The dimension and location of each cell is geometrically determined by the spot diameter, the overlap ratio and the alternating offset. Figure 3 a) features 16 shots and the induced origin and dimension of the representative cells. Figure 3 b) indicates the tessellation of the representative

cells on the surface of the target geometry: While corners stay unchanged in their dimension, edges get extended in one dimension and the center patch gets extended in two dimensions.

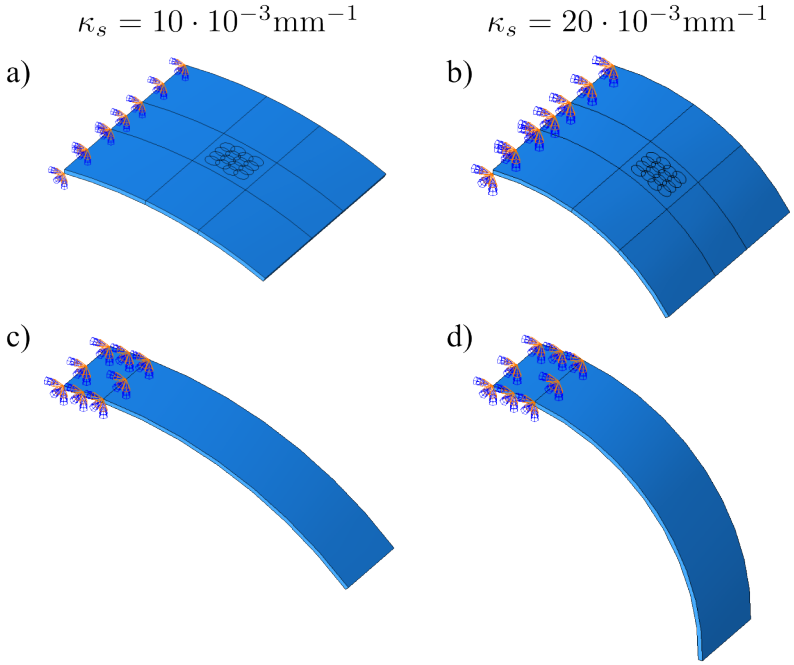

Figure 1: Investigated geometries with boundary conditions; a) source geometry of lowest curvature, b) source geometry with highest curvature, c) target geometry with lowest curvature, d) target geometry with highest curvature.

Pulse modelling. For an individual laser pulse, the pressure p, acting on the surface can be expressed as

$$p = p(x, t), \tag{3}$$

where vector $\boldsymbol{x}$ is a coordinate point on the surface and t is the time. In this work, the spatial distribution of the pressure pulse is assumed uniform, leaving only the temporal evolution. To model the rapid pressure rise caused by the plasma expansion and the following pressure decay, two time parameters t_{amp} and t_{70} were introduced, yielding

$$\begin{aligned} p(t_{amp}) &= p_{max} \\ p(t_{70}) &= 0.7\, p_{max} \\ p(t) &\propto exp(-t) \quad \text{for } t > t_{70}. \end{aligned} \tag{4}$$

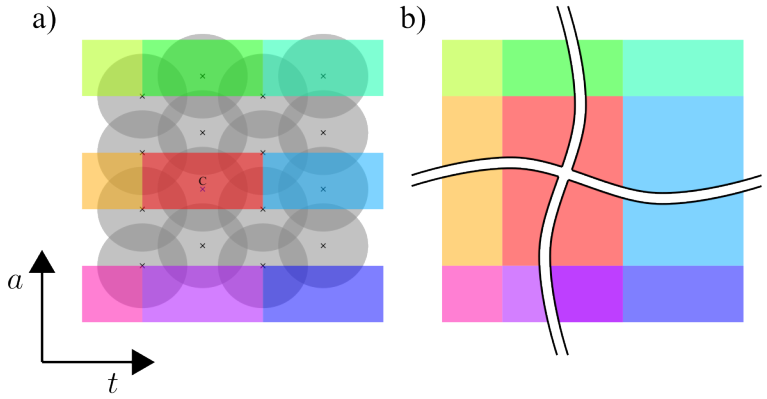

Figure 3: a) Representative cells with underlying peening pattern on the source geometry, b) tessellation with representative cells on the target geometry.

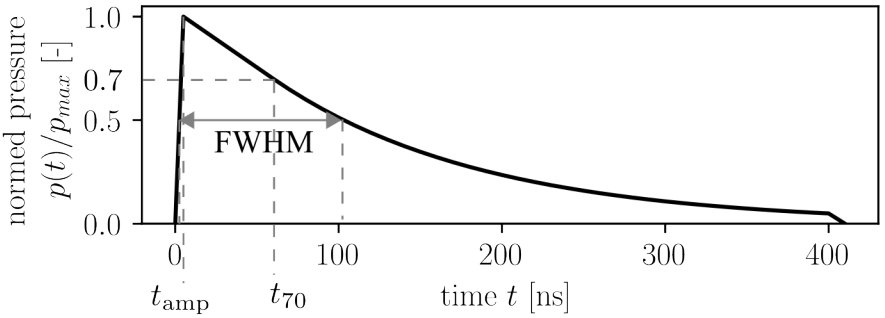

Figure 2: Temporal evolution of the pressure pulse.

The maximum pressure p_{max} applied in all simulations is chosen such that dynamic yielding results in defomations of >1 mm at the specimen's free tip. The exponential decay is truncated once 5% of the maximum pressure is reached. The timespan between reaching half maximum in the increasing phase and again in the decreasing phase is called *full width half maximum (FWHM)* and is well established in the literature. For the applied pulse it is 100 ns. Figure 2 shows the plot of this characteristic.

Material Model. The constitutive modelling of Ti-6Al-4V must account for the extremely high strain rate during laser processing [9]. The Johnson-Cook material model with neglected temperature term models the viscoplastic material behavior [10]. The governing equation reads

$$\sigma_y = \left[A_{JC} + B_{JC}\varepsilon_{BC}^{n_{JC}}\right]\left[1 + C_{JC}\ln\left(\frac{\dot{\varepsilon}_p}{\dot{\varepsilon}_{p,0}}\right)\right], \tag{5}$$

where ε_p respective $\dot{\varepsilon}_p$ is the equivalent plastic strain and its rate while A_{JC}, B_{JC}, C_{JC}, n_{JC} and $\dot{\varepsilon}_{p,0}$ are material parameters, listed for Ti-6Al-4V in Table 1.

Table 1: Elastic and Johnson-Cook material parameters for Ti-6Al-4V [11]

Density ρ, [g/cm³]	Young's modulus E, [MPa]	Poisson's ration ν, [-]	Yield strength A_{JC}, [MPa]
4.47	108500	0.33	728.7
Strain hardening coefficient B_{JC}, [MPa]	Strain hardening exponent n_{JC}, [-]	Strain rate hardening coefficient C_{JC}, [-]	Reference strain rate $\dot{\varepsilon}_{p,0}$, [s^{-1}]
498.4	0.28	$28 \cdot 10^{-3}$	$1 \cdot 10^{-5}$

Source simulation. The peening process is simulated using ABAQUS/Explicit. After each pressure pulse, a relaxation phase of 50 µs ensures the decay of transient behavior in the stress and strain fields. In all source simulations, the 16 spots are exposed to the pressure pulse in a spatial *zig-zag* order, meaning: The four shots of line 1 are irradiated from left to right; afterwards, the four shots of line 2 are irradiated from right to left; and so on. This is looped three times, resulting in three simulated peening sequences. After this explicit simulation, an implicit simulation is run

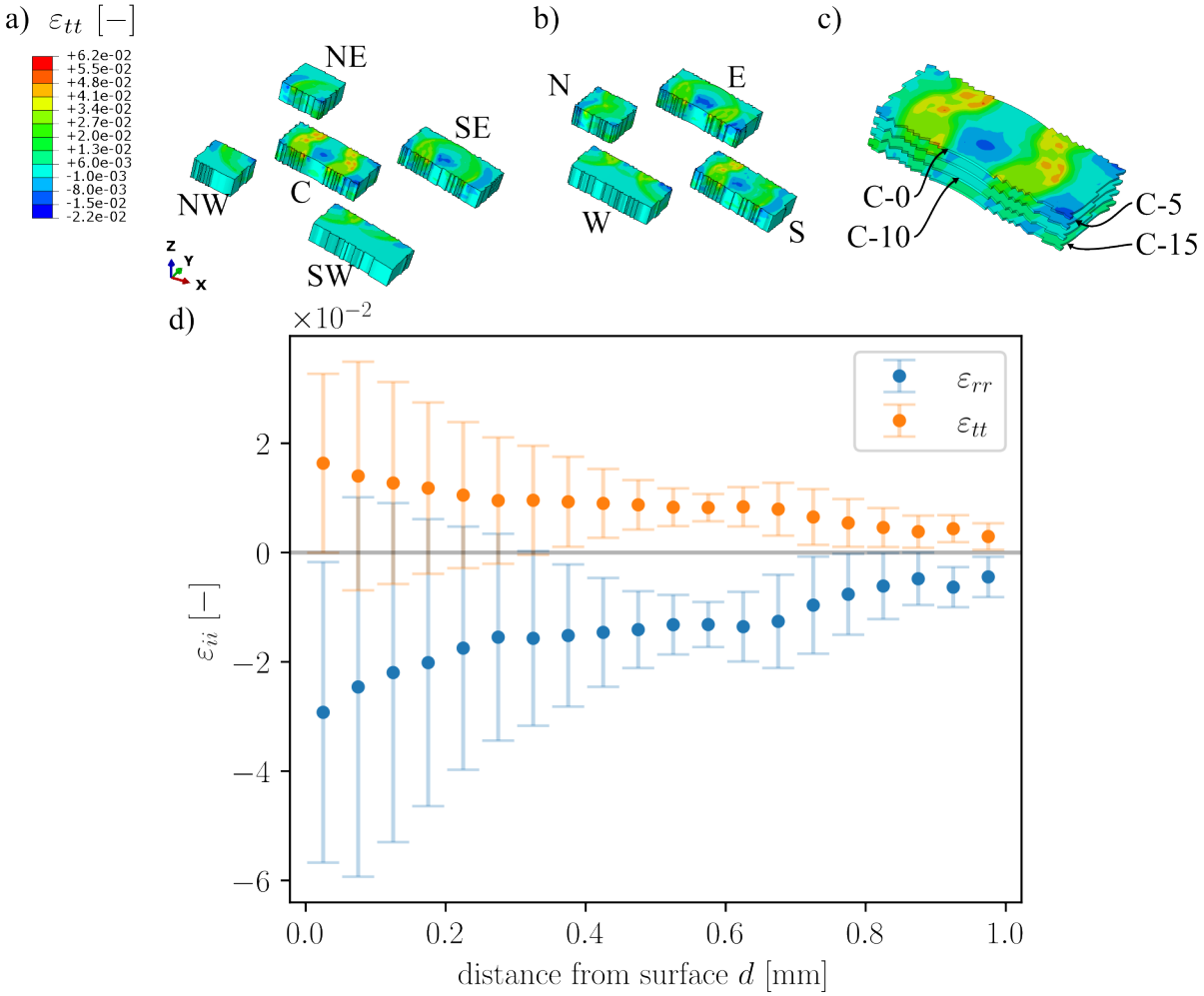

Figure 4: Tangential plastic strains for a) center and corners of wind rose patches, b) edges of wind rose patches (scale of a) applies) and c) 4 exemplary layers of center patch (scale of a) applies); d) radial and tangential plastic strains through thickness for center patch.

to reach equilibrium. The limited number of shots result in no significant deflection and therefore no change in the curvature of the source geometry.

Eigenstrain mapping. After the explicit and implicit simulation of the source geometry, the eigenstrains are determined in a *mid-processing* procedure. Each of the 9 representative cells is split into 20 in-depth slices, resulting a total of 180 slices. Based on the coordinate of the integration point, an element was assigned to one of the 180 slices or not. For all elements assigned to a certain slice, the plastic strain tensors were averaged using an element-volume-weighted averaging scheme. This resulted in one eigenstrain tensor for the whole slice and 180 eigenstrain tensors for the peening pattern. Figure 4 a) and b) show a stacking of the 20 in-depth cells for the 9 windrose patches while c) tries to indicate the stacking of 20 cells by showing 4 exemplary cells. Figure 4 d) shows the profile of the radial as well as tangential plastic strains for the center patch over all 20 slices. On the target geometry, based on the larger-scale peening pattern, the origin and dimensions of the representative cells were calculated. All elements were assigned to a cell according to the coordinate of the integration point as depicted in Figure 3 b). The elements were assigned the averaged eigenstrain as an anisotropic thermal expansion coefficient according to Eq. 1.

Target simulation. Once the eigenstrains have been introduced as thermal expansion coefficients, the simulation of a temperature increase of $\Delta T = 1K$ results in the deflection of the geometry as if a large number of individual shots in the large-scale peening pattern have been simulated. A curve $c(s)$ on the surface of the probe in the axial middle is determined based on data from the mesh nodes, where $s \in [0, \dots, 80]\, mm$ is the arc length of the curve starting from the encastre. In a cartesian coordinate system, the coordinates of the curve after deformation are parametrized as $c(s) = \big(x(s), z(s)\big)$ with the two scalar functions $x(s)$ and $z(s)$.

Cross-mapping and curvature calculation

The eigenstrain ansatz presumes that the eigenstrains originate from a domain that has identical properties as the domain where they are applied, e.g. material, thickness, orientation, etc. In this work, this presumption is investigated by cross-mapping of eigenstrains from and onto geometries with different curvatures. The eigenstrains from each of the 5 source geometries can be mapped onto each of the 5 corresponding target geometries, resulting in 25 simulations.

Let κ_s be the initial curvature of the source geometry and κ_t be the initial curvature of the target geometry, then the source curvature difference

$$\Delta\kappa_s = \kappa_t - \kappa_s \tag{6}$$

is defined as the curvature difference between the destination and origin of the eigenstrains. Figure 5 a) depicts three examples for $\Delta\kappa_s$ less than, equal to and greater than zero. Once $c(s)$ is extracted from the simulation results, the two functions $x(s)$ and $z(s)$ enable the calculation of the local curvature $\kappa(s)$ as

$$\kappa(s) = \frac{\dot{x}(s)\ddot{z}(s) - \ddot{x}(s)\dot{z}(s)}{(\dot{x}(s)^2 + \dot{z}(s)^2)^{\frac{3}{2}}}, \tag{7}$$

where discrete derivation is done via a central difference scheme. In terms of the arc length, the origin and dimension of the peening pattern is located at $s \in [17\text{mm}, \dots, 71\text{mm}]$. In order to get one scalar curvature for the whole deflected surface, the curvature after deflection $\bar{\kappa}_t$ is calculated as average over all discrete values for the curvature in this interval. To finally describe a difference of curvature deflection, one last quantity needs to be introduced: Let $\bar{\kappa}_{t,0}$ be the curvature after

deflection for the case where the eigenstrains originated from a source geometry with the same curvature. Then the target curvature difference $\Delta\kappa_t$ as a function of $\Delta\kappa_s$ is defined as

$$\Delta\kappa_t(\Delta\kappa_s) = \bar{\kappa}_t(\Delta\kappa_s) - \bar{\kappa}_{t,0}. \tag{8}$$

Figure 5 b) depicts the logic behind this definition.

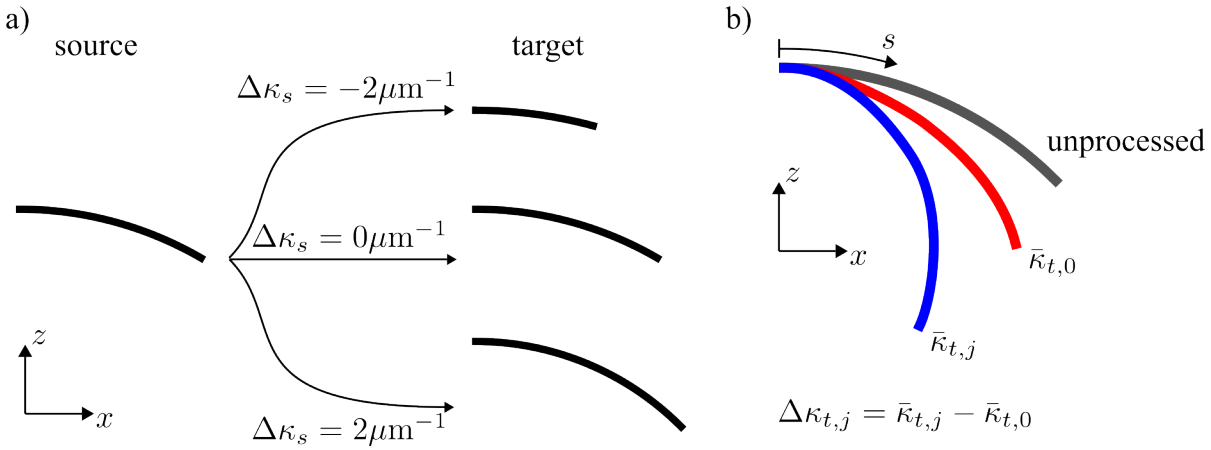

Figure 5: a) The origins of the source curvature difference $\Delta\kappa_s$ and the target curvature difference $\Delta\kappa_t$.

Results

In order to find a relation between the mapping curvature difference between and the reached induced curvature difference, a regression of the data was determined. Two constrains for the regression were set: $\Delta\kappa_t(0) = 0$ and $\Delta\kappa_t(\epsilon) \neq \Delta\kappa_t(-\epsilon)$ for $\epsilon > 0$. The linear regression of all data $\Delta\kappa_t(\Delta\kappa_s) = m(\Delta\kappa_s) + b$ with $b = 0$ and a value of m determined by a least squares error ansatz is chosen. This way, when the source curvature difference is zero, the target curvature difference is zero. The regression yields a value of the slope of $0 < m < 1$. Figure 6 plots the target curvature difference over the source curvature difference of the 25 simulations and the forced mean. The significant standard deviation of the data, indicated with the error bars, is due to the lack of preliminary smoothing before the discrete derivation and the following averaging process.

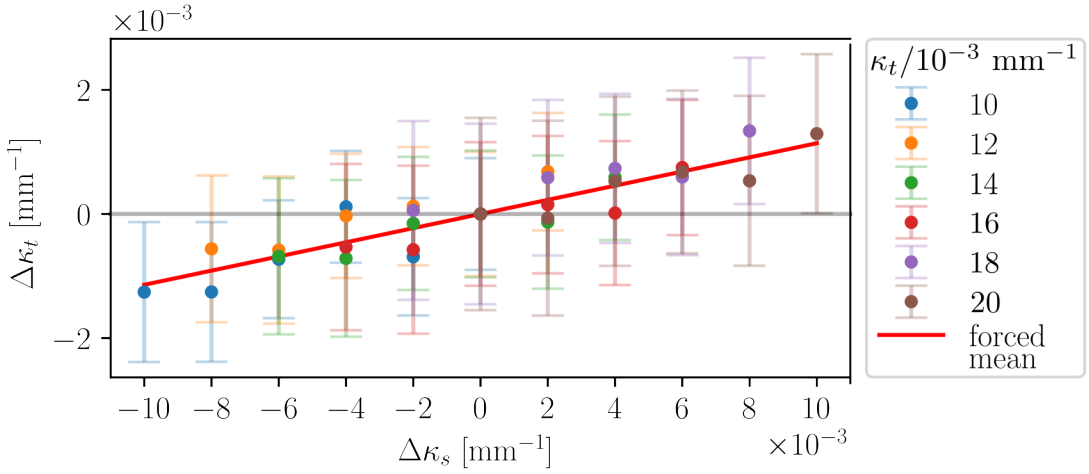

Figure 6: Target curvature difference against source curvature difference with forced mean relation.

The positive slope of the forced mean indicates the geometry dependence of the eigenstrains: For positive $\Delta\kappa_s$, the curvature change of the target geometry will be overstated; for negative $\Delta\kappa_s$, the curvature change of the target geometry will be understated. The value of $m < 1$ indicates a tolerance of the eigenstrain ansatz for deviations in the eigenstrain. While the data points stem from discrete values of cylinder shells with uniform curvature, the continuous relation is able to improve LPF simulations of geometries with a non-uniform, continuous curvature profile. In the following, two ways, how knowledge of this relation gives an advantage when simulating small forming operations, are outlined: Assume, a small forming operation on target geometry with a non-uniform curvature distribution $\tilde{\kappa}_t(s)$ should be simulated. If one eigenstrain tensor on a geometry with uniform curvature $\tilde{\kappa}_s$ is known, then the relation gives an estimate on the maximal error caused by using the one known eigenstrain tensor, explicitly

$$|\max(\Delta\kappa_t)| = m \max_s(|\tilde{\kappa}_t(s) - \tilde{\kappa}_s|) \tag{9}$$

Also, for a given target geometry with a non-uniform curvature distribution $\tilde{\kappa}_t(s)$, if the error in overall shape prediction needs to be limited to a given value, then the relation dictates the number of eigenstrain tensors n_ε needed to stay below a corresponding target curvature difference $\tilde{e}$, namely

$$n_\varepsilon = \left\lceil \frac{m\left(\max_s \tilde{\kappa}_t(s) - \min_s \tilde{\kappa}_t(s)\right)}{\tilde{e}} \right\rceil \tag{10}$$

The results are derived from geometries with a mono-directional curvature. No statement on geometries with multi-dimensional, non-trivial curvature can be made.

Conclusions

In this work, the simulation workflow using the eigenstrain ansatz was set up to model LSP processing of thin-walled Ti-6Al-4V specimen. For a smaller scale geometry, a small number of laser shots were simulated and the resulting eigenstrains were determined based on representative cells defined by the peening pattern. The eigenstrains were mapped onto a larger scale geometry featuring a large scale pattern. The introduced eigenstrains result in a global deflection curve, for which local curvatures and a global quantity as its proxy were calculated. The dependence of the induced curvature on the curvature of the origin of the eigenstrains was investigated.

The results yield a linear relation between the source curvature difference and the target curvature difference. This hints at a geometry sensitivity of the eigenstrains contrary to current literature. A possible explanation is the area moment of inertia, which in this case features an additional term due to Steiner's theorem. The higher the curvature of the geometry, the higher the axial area moment of inertia. This also yields: For identical radial load, a geometry with higher curvature will exhibit higher plastic strains than a geometry with lower curvature. For positive $\Delta\kappa_s$, mapped plastic strains that are lower than physically correct result in a deflection that is larger than physically correct, which corresponds to positive $\Delta\kappa_t$.

The results can be applied to the simulation of small forming operations of complex shaped parts: A known eigenstrain tensor can be used in a maximally large volume or the number of eigenstrain tensors needed can be estimated. For both cases, the gain in efficiency by use of the eigenstrain ansatz, compared to direct simulation, can be maintained.

Using the determined relation, future work of the authors will aim to investigate the simulation error that arises from the discretization of a target geometry with a continuous curvature in a given closed interval. A generalization to multidimensional curvature will also be tackled in upcoming work.

Acknowledgements
The work was carried out within the PEENCOR project funded by the German Federal Ministry of Economic Affairs and Climate Action (BMWK) under the LuFo VI-1 program (project numbers: 20Q1920C, 20Q1920D), which is gratefully acknowledged.

References

[1] R. R. Boyer, "An overview on the use of titanium in the aerospace industry," *Materials Science and Engineering: A*, vol. 213, no. 1, pp. 103–114, Aug. 1996. https://doi.org/10.1016/0921-5093(96)10233-1

[2] L. Berthe, R. Fabbro, P. Peyre, L. Tollier, and E. Bartnicki, "Shock waves from a water-confined laser-generated plasma," *Journal of Applied Physics*, vol. 82, no. 6, pp. 2826–2832, Sep. 1997. https://doi.org/10.1063/1.366113

[3] P. Peyre and R. Fabbro, "Laser shock processing: a review of the physics and applications," *Optical and Quantum Electronics*, vol. 27, no. 12, pp. 1213–1229, Dec. 1995. https://doi.org/10.1007/BF00326477

[4] Y. Hu and R. V. Grandhi, "Efficient numerical prediction of residual stress and deformation for large-scale laser shock processing using the eigenstrain methodology," *Surface and Coatings Technology*, vol. 206, no. 15, pp. 3374–3385, Mar. 2012. https://doi.org/10.1016/j.surfcoat.2012.01.050

[5] P. A. Faucheux, F. P. Gosselin, and M. Lévesque, "Simulating shot peen forming with eigenstrains," *Journal of Materials Processing Technology*, vol. 254, pp. 135–144, Apr. 2018. https://doi.org/10.1016/j.jmatprotec.2017.11.036

[6] S. Keller, M. Horstmann, N. Kashaev, and B. Klusemann, "Experimentally validated multi-step simulation strategy to predict the fatigue crack propagation rate in residual stress fields after laser shock peening," *International Journal of Fatigue*, vol. 124, pp. 265–276, Jul. 2019. https://doi.org/10.1016/j.ijfatigue.2018.12.014

[7] S. T. Sala, R. Körner, N. Huber, and N. Kashaev, "On the use of machine learning and genetic algorithm to predict the region processed by laser peen forming," *Manufacturing Letters*, vol. 38, pp. 60–64, Nov. 2023. https://doi.org/10.1016/j.mfglet.2023.09.006

[8] S. Cai and Y. Zhang, "A novel approach to reconstruct residual stress fields induced by surface treatments in arbitrary 3D geometries using the eigenstrain method," *International Journal of Solids and Structures*, vol. 236–237, p. 111372, Feb. 2022. https://doi.org/10.1016/j.ijsolstr.2021.111372

[9] Z. Zhou *et al.*, "Thermal relaxation of residual stress in laser shock peened Ti–6Al–4V alloy," *Surface and Coatings Technology*, vol. 206, no. 22, pp. 4619–4627, Jun. 2012. https://doi.org/10.1016/j.surfcoat.2012.05.022

[10] G. R. Johnson and W. H. Cook, "A Constitutive Model and Data for Metals Subjected to Large Strains, High Strain Rates, and High Temperatures. Proceedings of the 7th International Symposium on Ballistic," The Hague, Apr. 1983, pp. 541–547.

[11] W.-S. Lee and C.-F. Lin, "High-temperature deformation behaviour of Ti6Al4V alloy evaluated by high strain-rate compression tests," *Journal of Materials Processing Technology*, vol. 75, no. 1, pp. 127–136, Mar. 1998. https://doi.org/10.1016/S0924-0136(97)00302-6